J. Fluid Mech. (2020), *vol*. 905, A35. © The Author(s), 2020.
Published by Cambridge University Press
doi:10.1017/jfm.2020.755

Turbulent entrainment into a cylinder wake from a turbulent background

Krishna S. Kankanwadi[1],† **and Oliver R. H. Buxton** [1]

[1]Department of Aeronautics, Imperial College London, South Kensington Campus, London SW7 2AZ, UK

(Received 29 November 2019; revised 10 August 2020; accepted 8 September 2020)

The effects of background turbulence on the entrainment process, as well as the nature of the interfacial region between two bodies of turbulent fluid, were examined through an investigation of the far wake of a circular cylinder that is subjected to free-stream turbulence. Simultaneous particle image velocimetry and planar laser induced fluorescence measurements were conducted 40 diameters downstream of the cylinder. Despite the availability of turbulent, rotational fluid in the background, the outer interface between the wake and the ambient fluid exhibits an enstrophy jump akin to the classical result of a turbulent/non-turbulent interface. This jump at the wake boundary persists even when the intensity of the background turbulence is greater than the turbulence intensity of the wake itself. Analysis on the structure of the wake boundary reveals that an increase in background turbulence intensity results in an increased interfacial surface area relative to the non-turbulent case. However, instead of the intuitive result of increased entrainment as a result of increased surface area, a reduction in mean entrainment mass flux is observed with increased background turbulence intensity. Through the analysis of the flux probability density functions, the reduction in mean entrainment can be attributed to a tip in balance of extreme entrainment and detrainment events to the detrainment side in the presence of background turbulence. Lastly, a scale by scale analysis of entrainment behaviour revealed that free-stream turbulence affects entrainment behaviour across all length scales and is not just limited to the energy containing scales.

Key words: turbulent mixing, wakes

1. Introduction

Turbulent entrainment is the process by which mass is transferred into a body of turbulent fluid from the background. This process is of great significance as it defines the growth rate of regions encompassing turbulent fluid. Applications of this process are widespread and range from the growth of a turbulent boundary layer to the spread of an oil spill in an ocean. The rate of entrainment is effectively set by the dynamics near the outer boundary of these regions. The outer boundary is characterised by a sharp contorted interface of finite thickness. When surrounded by irrotational fluid, this boundary is referred to as the turbulent/non-turbulent interface (TNTI), and has been studied to a great extent at the edges of wakes, jets, mixing layers and boundary layers

† Email address for correspondence: krishna.kankanwadi12@imperial.ac.uk

(e.g. Bisset, Hunt & Rogers 2002; Westerweel *et al.* 2005). The pioneering work of Corrsin & Kistler (1955), made great strides into understanding the nature of the TNTI. They postulated the existence of a viscous 'superlayer', a zone where viscosity plays a central role in acting to transmit vorticity that is always present within the turbulent portion of the flow, to the irrotational background. They further proposed that the thickness of this layer is characterised by the Kolmogorov length scale, η, and, through dimensional arguments, that the propagation velocity of the layer is governed by the Kolmogorov velocity, $u_\eta = (\varepsilon\nu)^{1/4}$. Note, ε refers to the dissipation rate of turbulent kinetic energy and ν is the kinematic viscosity. These scalings have since been experimentally confirmed by Holzner & Lüthi (2011), who analysed a turbulent front generated by an oscillating grid. The zone just inside the viscous superlayer is termed the 'buffer layer' (Van Reeuwijk & Holzner 2013) and is responsible for the change in vorticity from the superlayer to the turbulent core. It is also a region where inertial effects dominate.

It is well known that turbulent entrainment is a multi-scale process. Townsend (1976) comments on the fact that the rate of entrainment is independent of the magnitude of fluid viscosity and the slow process of diffusion is accelerated through the interaction with all scales. Furthermore, commenting on how it is the large scales that control the rate of entrainment into a bounding surface between a turbulent and irrotational region, Sreenivasan, Ramshankar & Meneveau (1989) explain that large-scale motions are responsible for the creation of a larger interface surface area which in turn results in an increased rate of entrainment through small-scale viscous processes. Mistry *et al.* (2016) provide experimental evidence by showing that a balance is maintained between interface surface area and local entrainment velocity, in order to keep the overall mass flux as a function of length scale, constant.

A significant amount of work has gone into understanding the TNTI as well as entrainment from a non-turbulent environment, reviewed in da Silva *et al.* (2014). However, the process of entrainment when the background itself is turbulent is largely unexplored and poorly understood, whilst being highly relevant to a majority of industrial and environmental flows. The outer edge of the viscous superlayer in a TNTI is only defined in an arbitrary sense and represents an enstrophy iso-surface, where the rate of change of enstrophy is equal to zero. It is clear to see that the TNTI is defined by the lack of enstrophy present on one side of the interface. However, a large discrepancy in enstrophy either side of the interface is not a requirement for a turbulent–turbulent interface, with a change in mean momentum being the only constant for a turbulent shear flow exposed to a turbulent background. It may be possible that this interface is no longer an enstrophy iso-surface due to the dynamically evolving conditions on the free-stream side of the interface. In this study we aim to examine the structure of the bounding interface between the wake and the free-stream turbulence. However, prior to answering this, a zeroth-order question may be raised by reviewing comments of da Silva *et al.* (2014) on the interfacial region between two bodies of fluid hosting different levels of non-zero turbulence. This is to question if the turbulent–turbulent interface even exists? Therefore, the first priority of this study is to answer this zeroth-order question. It is worth noting that the TNTI is simply a special case of an interfacial region between two bodies that contain a differing level of turbulence in which one of the bodies is irrotational. However, this study aims to tackle the problem of the general case by investigating the boundary and studying the entrainment process between two regions of differing yet non-zero levels of turbulence. Literature on turbulent–turbulent entrainment (TTE) is scarce and only a few studies have examined it. Previous studies have highlighted the importance of two parameters of the free-stream turbulence to TTE, $\{L, u'\}$, respectively, the integral length scale and turbulence intensity.

Gaskin, McKernan & Xue (2004) investigated the near field of plane jets in a turbulent environment. They observed that once the turbulence intensity in the background was strong enough to disrupt the energy-containing eddies of the jet, the entrainment mechanism switched from large-scale engulfment to the small-scale process of turbulent diffusion. In this case the result was a suppressed rate of entrainment as a result of the background turbulence. Ching, Fernando & Robles (1995) also determined the dominant parameter to be u' in the free-stream turbulence (FST). In a study that observed turbulent line plumes subjected to FST, they were able to show a marked change in the spreading of the plume when the plume convective velocity, w_*, was comparable to the background turbulence intensity. They were also able to show that the plume was destroyed from the onset when $u' > w_*$.

Eames, Jonsson & Johnson (2011), on the other hand, demonstrated the influence of L, on the spreading rate of a cylinder wake. They concluded that in the absence of FST, the wake grew diffusively with respect to $x^{1/2}$, where x is the streamwise distance downstream of the cylinder. However, when FST was introduced and the velocity deficit decayed sufficiently such that it was comparable to u' of the ambient turbulence, Eames *et al.* explained that the wake grew linearly with streamwise distance when L was larger than the wake width. If this condition was not met, the wake continued to grow diffusively.

It is clear to see from current literature that L and u' both have a part to play in the physics behind TTE, although there is no consensus on the influence of each parameter and their respective sensitivities. Furthermore, the answer to the core question is unclear from the literature, that is, whether free-stream turbulence acts to increase or decrease entrainment relative to a non-turbulent background. Given two bodies with differing levels of non-zero turbulence, it may be reasonable to expect that fluid is entrained from a region of low turbulence to a region of higher turbulence. Behaviour similar to that suggested is evident in the space-scale unfolding mechanism between adjacent wakes in multi-scale generated turbulence postulated by Laizet & Vassilicos (2012) and experimentally verified by Baj & Buxton (2019). Therefore, to answer this core question on the effect of free-stream turbulence and to address the sensitivities of its parameters on the entrainment process, a systematic investigation exploring the effects of these parameters has been conducted in this study through the investigation of a wake behind a cylinder under the influence of free-stream turbulence, in which these parameters may be varied independent of each other.

The remainder of this manuscript is laid out as follows. The following § 2 details the experimental methodology used. We highlight the process of wake boundary identification in § 2.1 along with the verification of the methodology § 2.2. Section 3.1 provides details on the behaviour of the interfacial region when subjected to background turbulence and investigates if a turbulent–turbulent interface exists through the use of interface conditioned statistics. Section 3.2 analyses the geometry of the wake boundary itself. The entrainment flux calculation as well as the effects of free-stream turbulence on entrainment behaviour are discussed in § 3.3. Section 3.4 aims to deduce the relative influences of background integral length scale as well as turbulence intensity on entrainment behaviour. Finally, § 3.5 provides a scale by scale analysis on the effects of free-stream turbulence on the entrainment process.

2. Methodology

The experimental methodology consisted of simultaneous particle image velocimetry (PIV) and planar laser induced fluorescence (PLIF) experiments, and these were conducted

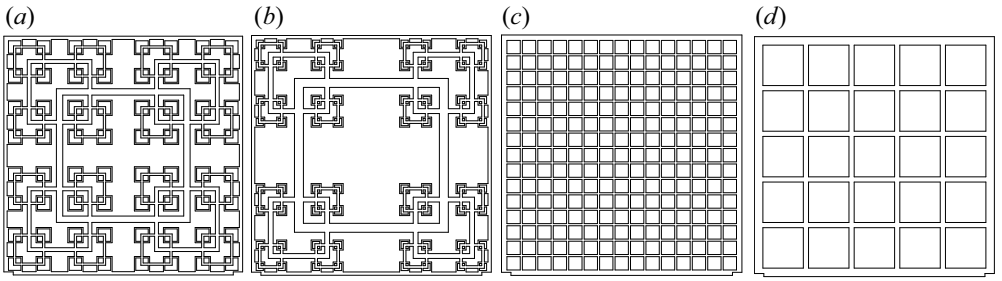

FIGURE 1. Schematic of turbulence generating grids: (*a*,*b*) display the square fractal grids, whereas (*c*,*d*) depict square regular grids. (*a*) SFG 5, (*b*) SFG 7, (*c*) SRG 38 and (*d*) SRG 111.

in a water flume with a working section length of 9 m and a cross-section of 600 mm × 600 mm, located at Imperial College London. A Reynolds number, based on the diameter d of the circular cylinder, Re_d, of approximately 4000 was achieved, hence placing the flow around the cylinder in the sub-critical regime (Williamson 1996). Note that the presence of the cylinder alone, resulted in a blockage ratio of just 1.7 %, thereby suggesting that wall effects may be considered negligible with respect to their impact on the entrainment behaviour downstream of the cylinder.

In this investigation, the incoming free-stream turbulence incident on the circular cylinder was produced by turbulence generating grids placed upstream of the circular cylinder. A total of four Perspex grids were manufactured and used. These grids were cut using 10 mm sheets of Perspex in a laser cutting facility. Two of the used grids were space filling square fractal grids (SFG), whereas the other two were square regular grids (SRG). The philosophy behind the design of these grids was to encourage the $\{L, u'\}$ parameter space to be as widely investigated as possible, in order to truly test the sensitivities of the entrainment process to both length scale as well as turbulence intensity. The flow downstream of all four grids was fully characterised and therefore the cylinder could be strategically placed at varying downstream distances so as to independently vary a single parameter in the background turbulence whilst the other remained constant. This followed the methodology of Melina *et al.* (2017). Tables 1 and 2 detail the design parameters of the fractal and square regular grids respectively, and figure 1 provides a schematic of all the turbulence generating grids. Note, T represents the width of the grid. In order to mount these grids in the flume they were encased in a frame and the blockage values specified in the table, σ, represent the true blockage of the grid as well as the encasing frame; N, is the number of fractal iterations; $\mathcal{L}_0$ and t_0 represent the length and thickness of the 'zeroth' iteration; $R_\mathcal{L}$ is the length ratio and R_t is the thickness ratio such that, $\mathcal{L}_j = R_\mathcal{L}\mathcal{L}_{j-1}$ and $t_j = R_t t_{j-1}$, where j is the scale iteration ($1 \leqslant j \leqslant N-1$). The suffix of the grid naming convention represents the ratio t_0/t_3 for fractal grids and $\mathcal{L}_0$ for regular grids. By way of illustration, grid 'SFG 5' is also sketched in figure 2, which details the experimental set-up used for a typical run.

Researchers have used several methods in the past to detect the location of the interface. The signature of a turbulent/non-turbulent interface is the large jump in enstrophy across the boundary. Therefore, a threshold on enstrophy is the most commonly found method of interface identification. Some of the other methods that may also be used are highlighted by da Silva *et al.* (2014). These include (a) analysing the probability density functions (PDFs) of vorticity at several points along the edge of the turbulent boundary, whilst searching for a shape change in the PDFs; (b) enacting a threshold based scheme on the turbulent kinetic energy; and (c) using a passive scalar as seen in the study by

Grid	T (mm)	N	$\mathcal{L}_0$ (mm)	t_0 (mm)	σ	R_L	R_t
SFG 5	569	4	312	15.3	33.76 %	0.477	0.591
SFG 7	569	4	354	21.5	34.50 %	0.389	0.533

TABLE 1. Fractal grids specification.

Grid	T (mm)	$\mathcal{L}_0$ (mm)	t_0 (mm)	σ
SRG 38	569	37.6	5.2	33.94 %
SRG 111	569	111.3	12.7	32.01 %

TABLE 2. Regular grids specification.

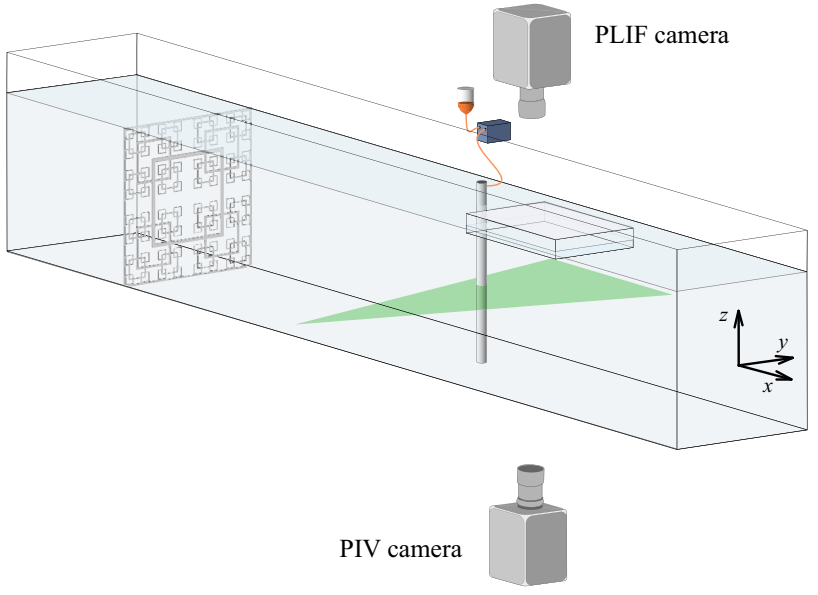

FIGURE 2. An example of the experimental set-up used for a typical run. The laboratory coordinate system is also shown. Note that, for clarity, the coordinate system has not been plotted on the origin (which lies on the rear face of the circular cylinder), instead it has been shifted downstream in the streamwise direction.

Westerweel *et al.* (2005). Since the aim of this study is to observe the entrainment behaviour in the presence of background turbulence, it is not possible to rely on enstrophy as a marker to identify the parts of fluid that constitute the cylinder wake. Due to the fact that rotational flow is present on both sides of the wake boundary, only (c) is applicable to this study. It is important to note that the passive scalar used must be of a high Schmidt number, Sc, which represents the ratio between the momentum diffusivity and the mass diffusivity. A high Sc ensures that diffusion is restricted to exceptionally small

Seeding	Type	Hollow glass spheres
Light sheet	Laser type	Nd:YLF
	Wave length	527 nm
	Frequency	1400 Hz
Camera	Model	Phantom v641 (x2)
	Resolution	1800 px × 2560 px
	Pixel size	10 μm
	Lens	Nikor 200 mm f/4 (PIV)
		Tokina 100 mm f/5.6 (PLIF)
Imaging	Viewing area	32.0 mm × 51.3 mm
	f_{aq}	225 Hz
	dt (PIV)	500 μs
	N_{aq}	2676
	Spatial resolution (PIV)	0.49 mm
PIV analysis	Interrogation area	24 px × 24 px
	Window overlap	50 %

TABLE 3. Experimental parameters used in this experiment. Note that f_{aq}, dt and N_{aq}, represent the acquisition frequency, the time separation between two frames of a single PIV burst and the total number of double frames captured.

length scales, meaning that the scalar faithfully tracks the fluid in the wake. Hence, a high Schmidt number scalar in the form of Rhodamine 6G was injected into the wake from the rear face of the cylinder in order to demarcate the wake from the free stream. A micro-dosing pump in the form of a Bürkert micro dosing unit 7615, operated at 10 Hz, was used to iso-kinetically release Rhodamine 6G into the cylinder wake. This pump discretely releases 5 μl of fluid per stroke and the flow output was smoothed by routing the released fluid through a 2 m long elastic tube that connected the pump to the release hole in the back of the cylinder. Rhodamine 6G has a Schmidt number of approximately 2500 in water (Vanderwel & Tavoularis 2014), making it an ideal candidate for use as a scalar in this experiment. Furthermore, tests conducted in a non-turbulent background examining the very near field of the wake that compared the extent of the scalar to the enstrophy distribution, confirmed that the released scalar was well stirred and faithfully marked the entire extent of the wake fluid. Therefore, this paper examines the entrainment process and the turbulent interface through a high resolution simultaneous planar PIV and PLIF experiment, conducted approximately 40 diameters downstream of the circular cylinder.

Figure 2 and table 3 depict the experimental set-up and provide a summary of the experimental parameters respectively. Illumination for both the PIV and PLIF experiments was provided by a Nd:YLF high-speed laser operating at 1400 Hz. Hollow glass spheres were mixed into the flow to be used as seeding particles for the PIV experiment. The nominal diameter of these particles is approximately 10 μm. Calculating the particle response time based on Stokes flow (τ_p) equates to 6 μs. For the particles to faithfully follow all the scales of fluid motion, the time scale with respect to the smallest eddies in the flow, the Kolmogorov time scale, τ_η, needs to be such that the Stokes number, $St_p = \tau_p/\tau_\eta \ll 1$. The resulting particle Stokes number was equal to 1.9×10^{-4}, hence indicating that the chosen seeding particles are appropriate.

Two Phantom v641 cameras were used to capture images during this study, one each for the PIV and the PLIF experiments. The PLIF experiment exploits the shifted emission

peak of Rhodamine 6G to allow the PLIF camera, along with the help of a low pass filter, to capture the tracer data whilst ignoring any seeded PIV particles. Rhodamine 6G has an absorption peak of 525 nm with an emission peak at a wavelength of 560 nm (Arcoumanis, McGuirk & Palma 1990). Hence the PIV camera was fitted with a bandpass filter centred around 532 nm, to prevent any reflected light from the dye affecting the PIV measurements. Table 3 also depicts the spatial resolution achieved during this experiment. A fine resolution of approximately 3η (0.49 mm), is necessary to capture the entrainment process in the inter-facial regions as this process is controlled by small-scale dynamics that scales with the Kolmogorov length scale (η).

Post-processing of all collected PIV images was done through a multi-pass cross-correlation method, which is implemented in the commercial PIV software offered by LaVision, DaVis. A total of three passes with a reducing window size were used to produce instantaneous velocity vectors. Images were also oversampled so that the overlap between two windows was equal to 50 %. A minimum peak ratio between the primary and secondary correlation peaks of 1.2, along with a median filter, were applied to reject spurious vectors. Any missing vectors were then interpolated. For all runs, the experimental PIV settings were optimised in order to keep the number of replaced vectors below 3 %. Post-processing for the PLIF experiment was done using in-house MATLAB codes.

Simultaneous PIV and PLIF experiments allowed for the scalar boundary to be used to identify the location of the wake boundary, from which conditional statistics were calculated. The process of interface identification is described in the sections below. At this stage it is important to note that, while the entrainment process is indeed three-dimensional, this study examines the process using two-dimensional experiments in a similar fashion to previous studies (Westerweel *et al.* 2005; Mistry *et al.* 2016). A two-dimensional experiment is needed to achieve a spatial resolution of the order of a few Kolmogorov scales, which is a necessity to resolve the entrainment process. Furthermore, due care has been taken to reduce the influence of three-dimensional effects, as highlighted in appendix C.

2.1. *Interface identification and treatment*

The metric used for interface identification in this paper relies on the magnitude of the gradient of light intensity present in the PLIF image. To use a simple light intensity threshold, as is seen in the literature, is not sufficient, since doing so assumes a consistent ejection of the dye at the nominal concentration along with a consistent power output from the laser source. These conditions are not usually met and result in a few eddies being illuminated with a greater brightness than others in the same field of view (FOV). Furthermore, a 'halo' effect caused by secondary fluorescence of the dye results in illumination of regions around highly concentrated blobs of the dye. This problem is highlighted and algorithmically resolved by Baj, Bruce & Buxton (2016). However, due to the nature of this phenomenon the 'halo' regions present a gradual variation in light intensity around bright spots. Hence, to avoid false detections, an identification metric that utilises the light intensity gradient magnitude as its input was deemed to be appropriate. This is mathematically defined as, $|\nabla\phi|$, where, ϕ is the light intensity of the PLIF image. Figure 13(a) depicts a typical image and the identified interface. The contour function in MATLAB is used to identify the longest continuous contour that satisfies the chosen threshold on the gradient metric. Similar to the interface treatment methodology of Mistry *et al.* (2016), pockets of scalar that are detached from the wake (as seen in the top right corner of figure 13a) are not considered in any further calculations. The ensemble of points

that are used for conditional analysis arrive from regions along an interface contour that satisfy a condition which prevents it from doubling back on itself. For each x-position, the contour is only allowed to exist at a single y location. In the case when multiple y-positions exist for a single x-position, only the data point that is furthest away from the turbulent core is used. This creates an 'envelope' of the interface and defines the ensemble of points used for further analysis.

2.2. *Methodology verification and threshold selection*

As with any study that utilises a threshold based method for interface identification, it is necessary to conduct a sensitivity study in order to appropriately select the threshold that faithfully identifies the interface. Figure 3(*a*) plots the mean value of enstrophy available in the regions not considered to be part of the wake for respective threshold values. Note that this result is for the test case of no grid, that is a TNTI, where we would expect to find minimal out of wake enstrophy. A jump in this value can be clearly seen in the range of threshold values that lie between -6 and -5. Note that the red line identifies the chosen threshold value of -5. This value is on the aggressive end of the range previously specified. Furthermore, choosing an aggressive yet appropriate threshold is necessary to combat and disregard the effects of secondary fluorescence. In order to further verify that the chosen threshold is appropriate, the conditional jump of enstrophy (ω^2) with respect to the normal distance away from the interface is plotted for several threshold values in figure 3(*b*). The enstrophy plotted in this conditional jump is averaged over the length of the interface present within the field of view (ξ) and also time-averaged over the ensemble of snapshots. Data processed in this manner are denoted with the following symbology, $\langle\rangle_I$. Note that γ represents the coordinate normal to the wake boundary, with positive γ representing the direction into the free stream. This coordinate transform from the laboratory coordinate system to the interface coordinate system is depicted in figure 4. The transformed coordinate system is then used in the calculation of all statistics that are conditioned by their distance to the wake boundary. Returning to figure 3(*b*), good convergence is seen in the region of the chosen threshold on the free-stream side of the wake boundary. Most importantly, the sharp jump in enstrophy is captured at the $\gamma = 0$ position, thereby confirming that the wake boundary has been accurately captured by our methodology. Furthermore, the successful implementation of our methodology over all experimental runs conducted in this study can be confirmed by referring to the conditional jump of light intensity (ϕ) with respect to the normal distance away from the interface. This plot is depicted in figure 3(*c*) and highlights the ability of the used methodology to capture the sharp rise in scalar at the $\gamma = 0$ position. After combining this result with that of the conditional enstrophy jump, it is possible to claim that this methodology is robust. Finally, it is to be noted that averaging over ξ is considered appropriate, since it is possible to associate a level of homogeneity with the background turbulence over the size of the field of view. From a Lagrangian perspective, in the far wake one might consider the turbulence to be somewhat 'homogeneous' over the distance advected during one eddy turnover time, $\tau \sim L_{12}/u'$, i.e. distance $\mathcal{L}_H \sim U_c\tau$, where U_c is the mean convection velocity. Taking $U_c = U_\infty$ and all constants of proportionality to be unity, the 'homogeneity length scale' $\mathcal{L}_H$ for all cases is larger than both dimensions of the field of view size ($\sim$3 cm $\times$ 5 cm). The smallest correlation distance that occurs in a background turbulence case equates to approximately 7 cm. Since this is sufficiently larger than the field of view size, we may be able to claim that the field of view is subjected to a level of homogeneity in all subjected background turbulence cases.

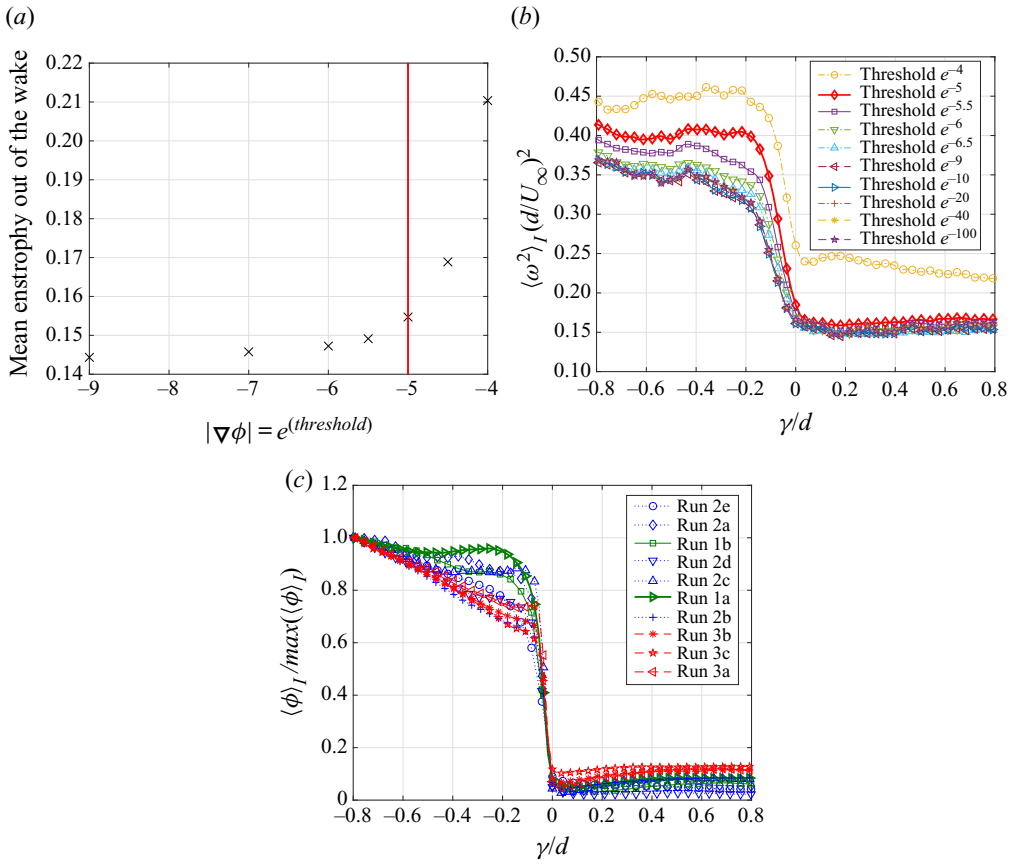

FIGURE 3. Threshold sensitivity study. Note, (*a*,*b*) refer to the no-grid case. (*a*) Plot showing the mean normalised enstrophy considered to be outside of the wake for varying gradient threshold values. (*b*) The variation of interface conditioned enstrophy jump for various threshold values. The thick red line represents the chosen threshold. Note that the boundary contour is different for each threshold value as the location of the contour is dependent on the threshold. (*c*) Interface conditioned plot of PLIF light intensity normalised by the maximum value for $-0.8 < \gamma < 0.8$, calculated using the chosen threshold value.

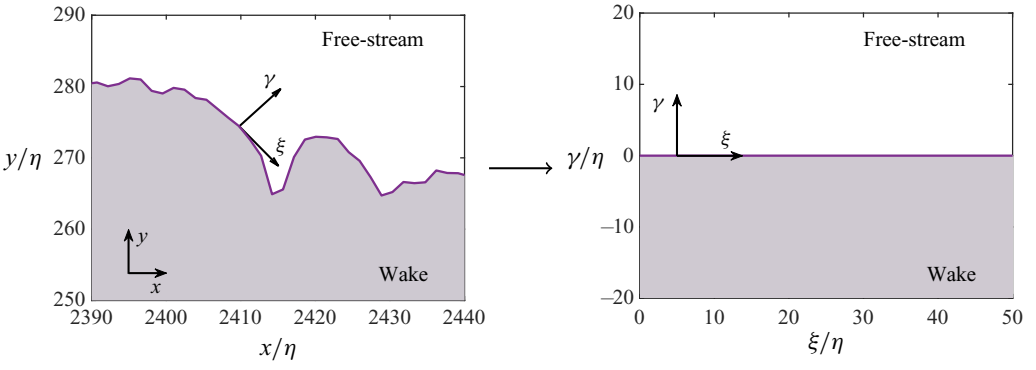

FIGURE 4. Schematic illustrating the coordinate transform employed to evaluate interface conditioned statistics.

2.3. *Calculating the background turbulence parameters*

Prior to addressing the results of this study, it is important to introduce the methodology of how the background turbulence parameters are calculated. All grids used in this study were fully characterised using PIV in a separate experimental campaign. These data were used to establish the background length scale as well as the background turbulence intensity that would be present at the location of the field of view of the current study. Appendix A provides figures that detail the flow downstream of each turbulence generating grid. Equations (2.1) and (2.2) mathematically define the integral length scale. The transverse auto-correlation function for the streamwise fluctuating velocity is represented by R'_{12}. Note that $r\boldsymbol{e_2}$ refers to some displacement r in the $\boldsymbol{e_2}$ direction, where $\boldsymbol{e_2}$ is a unit vector pointed along the y-direction. The length scale is then calculated by integrating the correlation function from zero to $\hat{r}$, where $\hat{r}$ is the location of the first zero crossing of the correlation function. Figure 5(*a*) depicts the auto-correlation function in the bulk flow in an empty tunnel. Calculating the integral length scale for 'no grid' placed upstream is not straightforward due to the presence of velocity correlation over a large distance, as would be expected for a predominantly laminar flow. However, an estimate for the integral length scale can be calculated by fitting an exponential to the short range correlation peak, producing a length scale estimate, L_{12}, of 3.4 mm. As a comparison figure 5(*b*) depicts a typical auto-correlation function that can be found downstream of a grid in turbulent flow. It should be noted that the length scale, L, may also be calculated in the streamwise direction or using the transverse fluctuating velocity. However, for the purposes of this study, L_{12} will be used to assess the length scale in the background. Finally, (2.3) provides a definition for the turbulence intensity. In this equation, u' and v' represent the fluctuating velocity in the streamwise and transverse directions, whereas, U_∞ represents the mean velocity in the free stream subjected to the circular cylinder. It is important to highlight that the fluctuating velocity, the integral length scale as well as the mean velocity subjected to the cylinder were measured through independent grid characterisation runs that were conducted without the cylinder mounted in the flume.

$$R'_{12}(\boldsymbol{x}, r) = \frac{\langle u'_1(\boldsymbol{x}) u'_1(\boldsymbol{x} + r\boldsymbol{e_2})\rangle}{\sqrt{\langle {u'_1}^2(\boldsymbol{x})\rangle}\sqrt{\langle {u'_1}^2(\boldsymbol{x} + r\boldsymbol{e_2})\rangle}}, \tag{2.1}$$

$$L_{12} = \int_0^{\hat{r}} R'_{12}\,\mathrm{d}r, \tag{2.2}$$

$$TI = \frac{(u'^2 + v'^2)^{1/2}}{U_\infty}. \tag{2.3}$$

3. Results and discussions

The effects of free-stream turbulence are twofold. On the one hand, the near field is affected since the shedding mechanism of the cylinder is disrupted by the incoming turbulence (Sadeh & Brauer 1980; Kwok 1986). Additionally, L and u' in the free stream also have a direct effect on entrainment into the wake, downstream of the near-wake region. This paper will focus on the latter.

Experiments were conducted in the far wake ($37 \leq x/d \leq 41$) in order to quantify the effects of free-stream turbulence on the entrainment process. Figure 6 illustrates the free-stream turbulence parameter envelope of this study. Note that the background free-stream turbulence intensity of the facility is equal to 1.4 %, and is representative of

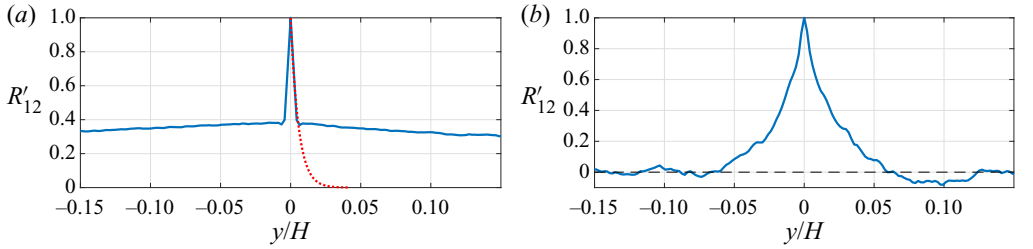

FIGURE 5. Transverse correlation function for streamwise fluctuating velocity. (*a*) Correlation function in an empty tunnel. Note that the dashed red line represents the exponential fitted to the short range correlation peak. (*b*) Typical function downstream of a turbulence generating grid. Note, H represents the width of the flume's working section.

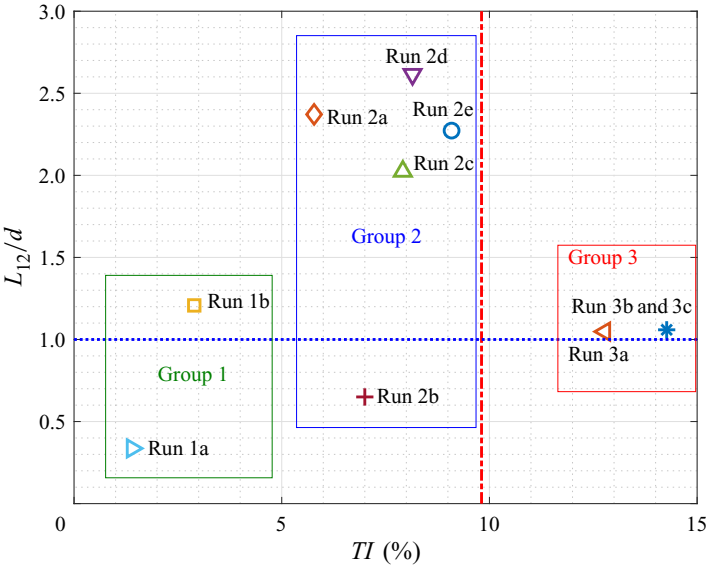

FIGURE 6. Free-stream turbulence parameter envelope. Note that the red dot-dashed line indicates the turbulence intensity near the centreline of the wake in the no-grid case, whereas the dotted blue line indicates a length scale equal to 1 cylinder diameter.

the amount of residual turbulence intensity in our control case ('no grid' run 1a). The nine remaining runs span a turbulence intensity, TI, space from 2 % to 14 %, with length scales varying from 0.3 up to 2.6 cylinder diameters. In addition to describing the parameter space, figure 6 also highlights the three main groups that have been distinguished amongst all conducted runs. Runs have mainly been categorised as a result of their entrainment behaviour and also the incoming free-stream turbulence intensity. The characteristics of each of these groups will be discussed in § 3.3. However, it is useful to introduce these groups at this stage of the manuscript. It should be noted that the naming convention used to identify each run indicates both the group the run belongs to, as well as the relative strength of the background turbulence intensity. The former is described by the numeral indicating the group number (run #x). Whereas the strength of the incoming turbulence intensity subjected to the cylinder is depicted in hierarchical order within each group using a single letter of the Latin alphabet (run #*x*).

3.1. *Evidence for the existence of the turbulent–turbulent interface: interface conditioned statistics*

Figures 7 and 8 depict interface conditioned statistics as a function of distance normal to the wake boundary (γ). (Note that the wake boundary is analogous to the turbulence/irrotational boundary in the case of a TNTI and is defined as the edge of the scalar extent. It corresponds to $\gamma = 0$.) As explained in § 2.2, data presented in these figures are averaged over ξ over the extent of the field of view and also time-averaged over the ensemble of snapshots, thereby represented with the following symbology, $\langle\rangle_I$. Figure 3(c) depicts the light intensity in the near vicinity of the wake boundary. The sharp increase in intensity around $\gamma = 0$ indicates a successful implementation of the gradient based interface identification methodology. For all runs the scalar boundary is successfully identified and further used to calculate interface conditioned statistics. Figures 7 and 8(a), depict mean normalised enstrophy and streamwise velocity as a function of distance normal to the wake boundary. The no-grid control case reproduces expected behaviour for both interface conditioned enstrophy as well as the streamwise velocity jump (da Silva *et al.* 2014). The base level of enstrophy rests at a non-zero value in the free stream. This is as a result of the residual free-stream turbulence present in the facility. With the introduction of background turbulence, we find that the classical TNTI result of an enstrophy jump at the interface is still present when turbulence is available on both sides of the interface. This is a crucial result as it goes to show that analogous to the TNTI, there exists a turbulent/turbulent interface at which enstrophy adjusts between the two fluid regions. As expected, the base level of enstrophy, as seen on the free-stream side of the interface, increases with added background turbulence intensity. For a majority of the grid turbulence cases, an extension to the magnitude of the enstrophy jump across the interface is seen. When the background turbulence becomes extreme and the intensity becomes greater than that of the wake, as is the case for runs 3a, 3b and 3c, an enstrophy jump is still present and the interface does not break down in a mean sense. Although the magnitude of this jump across the interface reduces in size as a severe increase is observed in the enstrophy available in the free-stream side of the interface.

Figure 8(a) depicts the mean streamwise velocity jump across the interface. As long as the turbulence is not too dominant, an increase in the mean shear rate by 40 % relative to the no-grid case is observed at the turbulent–turbulent interface. This value represents the mean increase in linear gradients that are evaluated by fitting to data points that reside inside the wake ($\gamma/d < 0$), calculated for runs that lie in groups 1 and 2. When rotational fluid is available on both sides of the interface, we expect the only consistent fluidic 'marker' of the wake to be time-averaged low momentum fluid. However, in runs 3b and 3c this property is no longer seen due to the extreme nature of the free-stream turbulence. Despite the loss of a mean-momentum jump across the interface in these cases, it is interesting to observe that an enstrophy jump is still present even though the turbulence intensity in the free stream is higher than in the wake. The nature of these cases that reside in group 3 will be explained further in the following sections.

The conditional jumps of turbulent kinetic energy are depicted in figure 8(b). It is possible to note that none of the jumps are explicitly stronger than the no-grid case. Furthermore, these jumps disappear for the group 3 cases. Therefore, it may be possible to speculate that transport is the major source term of turbulent kinetic energy in the vicinity of the wake boundary, be it pressure strain or turbulent diffusion. However, this is simply speculation at this stage as it lacks requisite evidence.

In a study examining the turbulent/non-turbulent interface, Buxton, Breda & Dhall (2019) showed an increase in small-scale anisotropy in the interface region. They examined

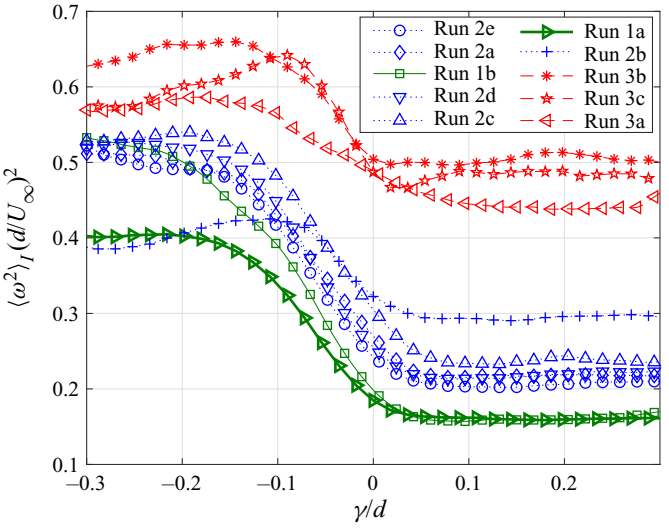

FIGURE 7. Interface conditioned normalised enstrophy as a function of normal distance away from the wake boundary. Note, throughout the manuscript run 1a (in bold) refers to the no-grid case.

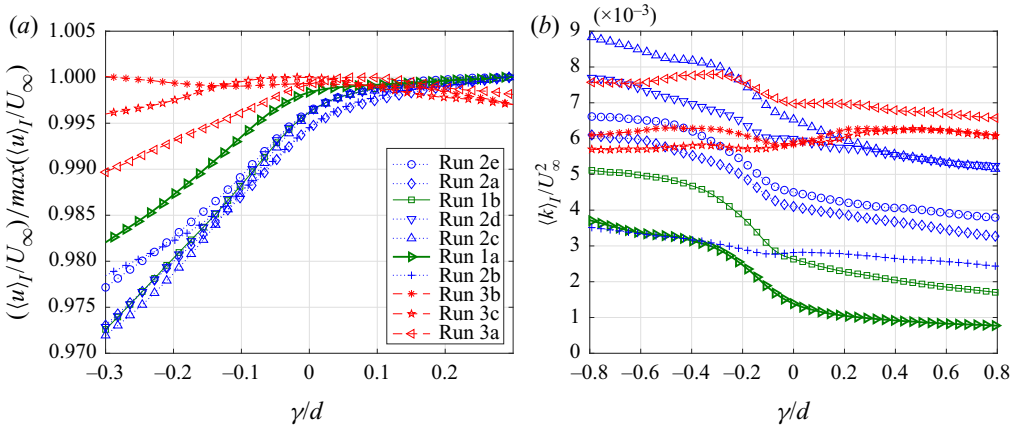

FIGURE 8. Interface conditioned statistics as a function of normal distance away from the wake boundary. (*a*) Normalised mean velocity; u and U_∞ refer to the streamwise velocity and the streamwise mean velocity, respectively. (*b*) Turbulent kinetic energy, k, normalised by U_∞^2.

the behaviour of the anisotropy ratio, Σ, as defined by, $\Sigma = \langle(\mathrm{d}u'_\gamma/\mathrm{d}\gamma)^2\rangle/\langle(\mathrm{d}u'_\xi/\mathrm{d}\xi)^2\rangle$ on the turbulent side of the boundary. The velocities represented in this equation are in the interface coordinate system, with u_γ and u_ξ corresponding to the velocity perpendicular to and parallel to the wake boundary, respectively. In isotropic flows this ratio is equal to unity. Hence, any deviation from unity reflects anisotropy in the flow. Figures 9(*a*) and 9(*b*) depict the behaviour of Σ for runs that belong to groups 1 and 2 and group 3, respectively. The no-grid case, as described by run 1a, produces results that are similar to those of Buxton *et al.* (2019), with an increase in anisotropy being observed near the wake boundary on the wake side of the interface. A very gradual increase in the anisotropy ratio

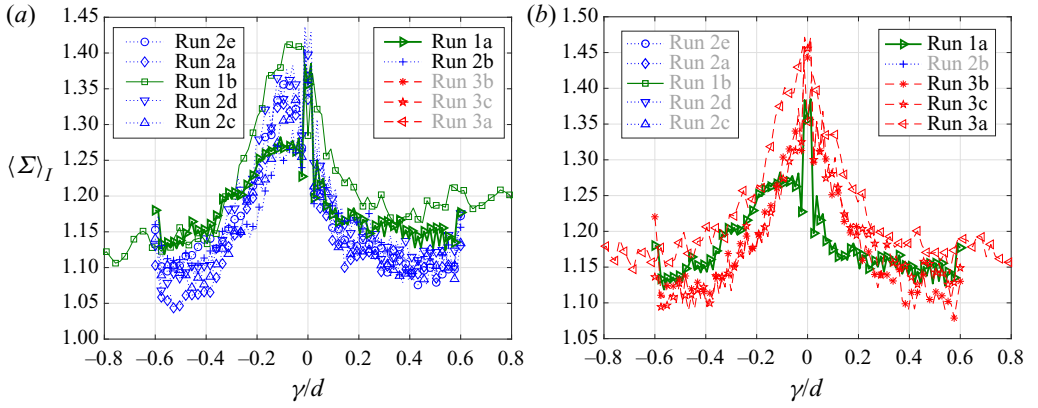

FIGURE 9. Interface anisotropy for turbulence cases in (*a*) groups 1 and 2 and (*b*) group 3.

is also observed on the free-stream side of the wake boundary, however, the magnitude of this increase in not comparable to the behaviour inside the wake.

Free-stream turbulence cases in both groups 1 and 2 express similar behaviour to the no-grid case, although the anisotropy level very close to the wake boundary is at a higher level when compared to the value inside the wake. The asymmetry caused by an increased bias to anisotropy on the wake side of the boundary is maintained in cases that belong to groups 1 and 2. However, this does not apply for group 3 turbulence, as can be seen in figure 9(*b*). A greater level of symmetry is evident in the anisotropy gain on both sides of the wake boundary. This may be expected due to the nature of the highly turbulent ambient flow in these three cases. As will be further explained in § 3.3, cases in group 3 consider an extreme case of incoming turbulence intensity as they examine the intersection of the cylinder wake with a strong wake created by the turbulence generating grid. The presence of strong turbulent wake-like behaviour on both sides of the wake boundary leads to a symmetrical increase in anisotropy as we approach the boundary. This behaviour is hypothesised to be responsible for the jump in enstrophy that is seen at the wake boundary for all tested cases, even when the intensity in the background is greater than the turbulence intensity inside the wake. This jump is hypothesised to be caused by the strong vorticity–strain interactions that manifest due to the increased anisotropy, which itself is a result of the increased strain rate in the interface normal direction within the vicinity of the wake boundary. The increased local strain rate naturally leads to an increase in the inviscid vortex stretching term of the enstrophy transport equation which can lead to it acting as an additional source of enstrophy which would not exist in a non-turbulent background. Mathematically, the vortex stretching term is defined as, $\omega_i S_{ij} \omega_j$, where, ω_i, ω_j are components of the vorticity vector and S_{ij} refers to the strain-rate tensor. Furthermore, it is highly likely the increase in anisotropy on both sides of the interface is only part of the story. It is not simply the magnitude of the strain-rate tensor, but also the alignment between the strain-rate tensor and the vorticity vector that determines the level of inertial enstrophy production. To show this, Betchov (1956) decomposed the production term as, $\omega_i S_{ij} \omega_j = \omega^2 s_i (\hat{\boldsymbol{e}}_i \cdot \hat{\boldsymbol{\omega}})^2$, where $\hat{\boldsymbol{e}}$ and $\hat{\boldsymbol{\omega}}$ are unit vectors pointing in the direction of the strain-rate eigenvectors and the vorticity vector respectively. It is then possible to explain that the enstrophy production is determined by the cosines of the alignment angle between the principal axes of the strain-rate tensor and the vorticity vector. In the case of a turbulent/non-turbulent interface, Elsinga & da Silva (2019) show preferential alignment

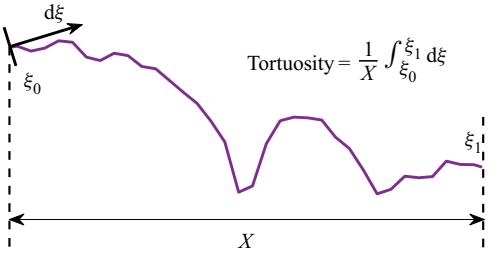

FIGURE 10. Illustration of methodology used to calculate tortuosity.

of the vorticity vector and the most stretching strain direction at the irrotational boundary. Watanabe *et al.* (2014) also highlight boosted enstrophy production in the vicinity of the interface when turbulent fluid moves toward the TNTI. Bearing this in mind, it is possible to postulate that the vorticity in the wake is more likely 'organised' than in the background, leading to an increased enstrophy production despite the symmetrical anisotropy distribution. This could therefore be the mechanism by which the enstrophy jump is preserved in strongly turbulent background conditions.

3.2. *Tortuosity*

Tortuosity defines the level of contortion of the interface. Mathematically, we define this as the ratio of the length of the wake boundary to the distance between its two ends (see figure 10). A sensitivity study to the input parameters reveals the dependence of the tortuosity value on the turbulence intensity. An increase in intensity of the incoming free-stream turbulence resulted in a more tortuous interface. Figure 11 displays the scatter with respect to subjected integral length scale and turbulence intensity. Reviewing the PDFs (figure 12) shows wider peaks that are shifted to the right in the presence of any incoming grid turbulence, highlighting the prevalence of intermittent high magnitude events along with a modal shift towards a higher tortuosity value. Hence, this result goes on to suggest an increased interface surface area with added background turbulence. It is important to note that the tortuosity calculations have been conducted on the 'un-treated' wake boundary. In other words, the conditionality that prevents the contour from doubling back on itself does not apply here. This ensures that the result being presented in figures 11 and 12 are not unduly biased by any interface treatment methodologies that are in place to facilitate the calculation of the entrainment mass flux.

3.3. *Entrainment mass flux*

The motion of the interface is governed by two distinct phenomena. On the one hand, local fluid advects turbulence in space, whereas fluid from the background is also entrained into the wake, causing it to grow in size. The latter is controlled by the local entrainment velocity, V_γ, the calculation of which, requires knowledge of both the time-resolved instantaneous location of the interface as well as the background fluid velocity. The process to evaluate the entrainment velocity is similar to the one used by Mistry *et al.* (2016) and the steps are listed below. Figure 13 graphically depicts the process.

(i) Local fluid velocity u_0: the local fluid velocity is acquired from the nearest grid point for each point along the contour at time t_0 (see figure 13*a*).

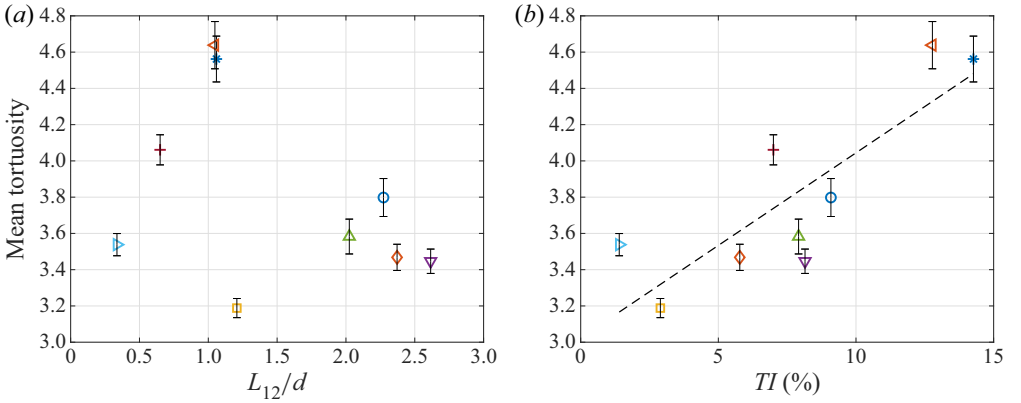

FIGURE 11. Plots depict the variation of interface tortuosity as a function of subjected turbulence's (*a*) integral length scale and (*b*) intensity. The dashed line indicates a linear regression fit. The error bars represent a 95 % confidence interval.

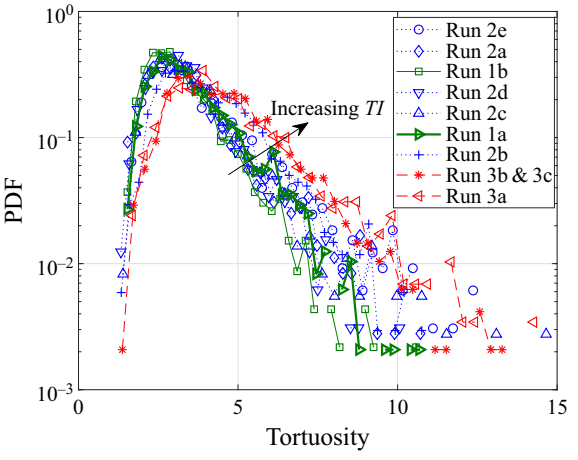

FIGURE 12. Probability density function for interface tortuosity for all subjected turbulence cases.

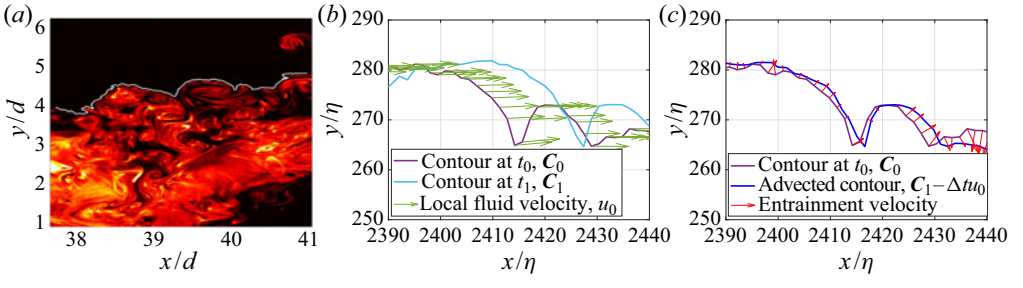

FIGURE 13. (*a*) A typical PLIF image. The solid white line represents the interface as identified by the gradient metric. (*b*,*c*) Plots depict the entrainment velocity calculation process. Note that η represents the Kolmogorov length scale.

(ii) Advection subtraction: contour at time, t_1, ($\boldsymbol{C}_1$), is identified and subtracted for local advection. Each point in $\boldsymbol{C}_1$ is subtracted by the vector $\Delta t\boldsymbol{u}_0$, where Δt is the time interval between two snapshots (see figure 13*b*).

(iii) Entrainment velocity: the normal distance with respect to the original contour, $\boldsymbol{C}_0$, to the advection subtracted contour, $\boldsymbol{C}_1 - \Delta t\boldsymbol{u}_0$, is used to calculate the entrainment velocity. A graphical method, as illustrated by figure 13, is used to ascertain the normal distance from each point on the original contour to an interpolated point along the advection subtracted contour. Note: in addition to this graphical approach, a point to point based methodology to calculate the entrainment velocity was also trialled and both methods produced comparable results.

Integrating the entrainment velocity along the interface produces a value for the mass flux entrained into the wake (see (3.1)). Note that this value is normalised by the cylinder diameter, d, and the incoming free-stream velocity, U_∞. Since the fluid in the flume is incompressible, the density term has been neglected from the equation below:

$$\textit{Normalised Mass Flux} = \frac{1}{d \times U_\infty} \int_0^s V_\gamma \cdot \mathrm{d}\xi. \tag{3.1}$$

Entrainment flux is calculated as a mean over the entire ensemble of captured snapshots for each turbulence case and the behaviour is examined against the input turbulence parameters. Figure 14(*a*) depicts the variation of the mean flux with input turbulence intensity. Considering all cases, a negative correlation can be observed, leading to an assertion that an increase in background turbulence intensity acts to reduce the rate at which background fluid is entrained into the wake. This seems to be an unintuitive progression, following on from the tortuosity result. We observe a reduction in entrainment flux despite the increased interface surface area (due to increased tortuosity) when the cylinder is subjected to incoming grid turbulence. This information alone proves that turbulent diffusion is not solely responsible for entrainment in the turbulent–turbulent entrainment paradigm. However, an explanation to this counter-intuitive behaviour can be attained by examining the probability density function of the normalised flux (see figure 15). The collection of subjected turbulence cases can be split into three distinct groups. Group 3, as highlighted in figure 14(*a*), represents extreme cases of incoming turbulence intensity. These cases have a severely reduced amount of entrainment into the wake, with run 3a displaying net negative entrainment (detrainment). The reduction in net entrainment can be explained by examining the balance between the highly intermittent, positive and negative, extreme entrainment events. A balance between these intermittent events is essential in maintaining a net positive-entrainment rate. Graphically, these events are represented by the tails of the flux PDF, shown in figure 15(*b*). All runs in group 3 witness a substantial boost to powerful negative-entrainment (detrainment) events. Furthermore, in the case of run 3a, there is also evidence of slight suppression of positive extreme entrainment events, which is not present for runs 3b and 3c. The significant amount of background turbulence that is available for cases in group 3 tip this balance towards the negative side. Thereby overcoming the increased amount of entrainment that should be expected due to the increased interfacial surface area, hence resulting in a large reduction in net entrainment. Evidence for such behaviour is also present in the reduced skewness values for both these cases in group 3. It is to be noted that the large amounts of background turbulence results in a wake that is highly intermittent, causing the location of the wake boundary to move significantly in the transverse coordinate. Therefore, due to the particularly small field of view used in this experiment, the sample size of snapshots that capture the wake boundary in full is significantly reduced (the percentage of valid

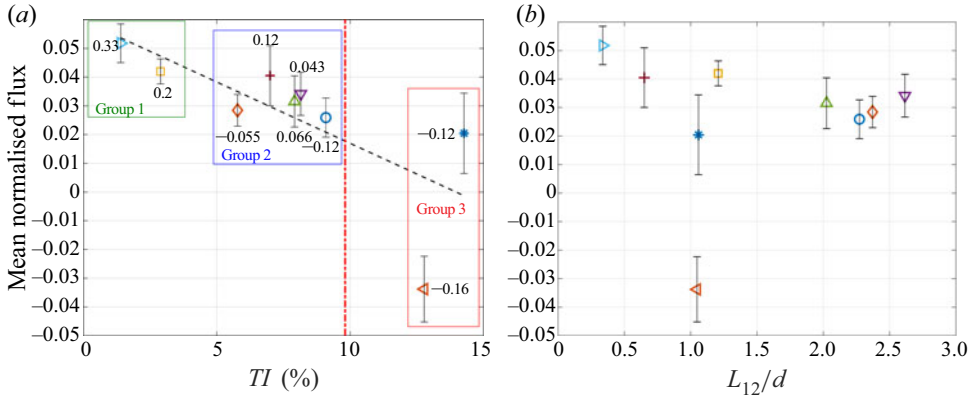

FIGURE 14. Entrainment mass flux as a function of (*a*) subjected free-stream turbulence intensity and (*b*) length scale (positive value indicates entrainment into the wake from the background). The dashed line indicates a linear regression fit. Text next to each data point indicates the skewness of the respective dataset. The error bars represent a 95 % confidence interval. The red dot-dashed line indicates the turbulence intensity near the centreline of the baseline (no-grid) wake.

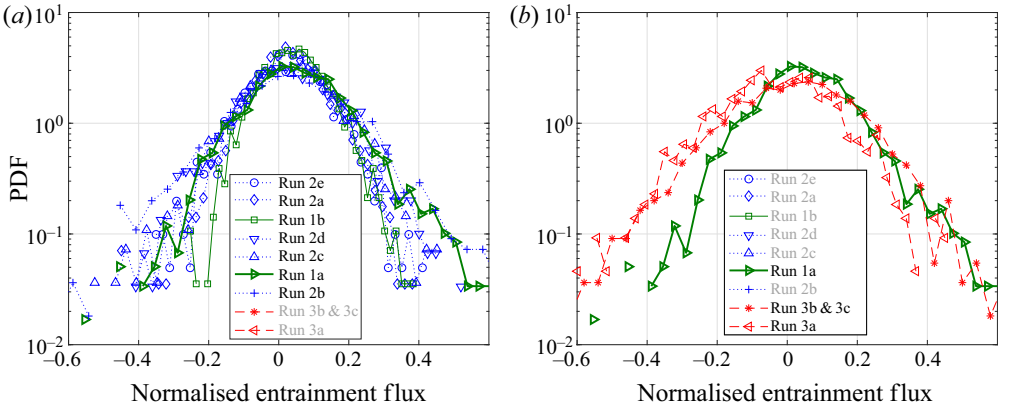

FIGURE 15. Probability density function for entrainment flux for (*a*) groups 1 and 2 and (*b*) group 3.

snapshots for run 3a which lies in group 3 is equal to 30 %, which is significantly lower than the no grid case that boasts 67 % of its total snapshots to be valid. Appendix C details how a snapshot is considered to be valid or invalid.). This phenomenon, along with the large intermittency found in this group, is responsible for the large confidence intervals for this group. Furthermore, it is to be noted that the mean value here is not a fully converged statistic as it will be highly dependent on the number of powerful intermittent events that are captured within the short acquisition time.

When the background turbulence intensity is not as overpowering as in group 3, the behaviour is slightly different. Group 2 presents a slight loss in entrainment, however, the wake still has a net positive mean entrainment mass flux (see figure 14*a*). Observing the PDFs for group 2 as depicted in figure 15(*a*), it can be seen that all cases in this group, with the exception of run 2b, display suppressed right tails. Whereas the left tail remains similar

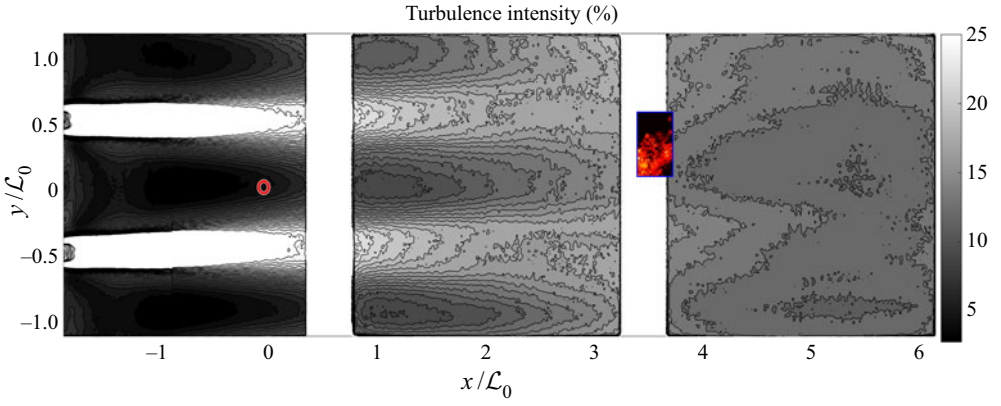

FIGURE 16. Turbulence intensity profile downstream of a square regular grid with $\mathcal{L}_0 = 111$ mm. The overlay represents the investigated FOV. The positioning of the grid, cylinder and the experimental FOV is consistent with that of runs 3b and 3c. Note that similar figures depicting the flow downstream of all grids used in this study can be found in appendix A.

to that of the no-grid case. Furthermore, all cases in this group also present a substantially reduced skewness value. Hence, highlighting a slight shift in balance towards detrainment events, explaining the reduction in mean entrainment mass flux. Note, although run 2b does present a lower mean entrainment value when compared to the no-grid case (run 1a), it does not share the PDF behaviour highlighted above. Additionally, the larger confidence intervals also indicate a larger standard error. Visual inspection of the PLIF images reveals the possibility that both of these characteristics are a result of increased entrainment in the out of plane component.

Finally, group 1 consists of cases that provide a low amount of incoming free-stream turbulence intensity, including the no-grid case. This group is characterised by a large and positive value of skewness and a net positive-entrainment mass flux into the wake.

Runs 3a, 3b and 3c display a negative and a largely reduced mean entrainment flux respectively. This remains a physical result as the geometry of these cases place the field of view in a region that investigates the interaction between two strong wakes. Figure 16 displays the turbulence intensity profile downstream of the regular grid as well as the location of the field of view for runs 3b and 3c. All three cases are in the near vicinity ($x/\mathcal{L}_0 < 7$) of a square regular grid, meaning that the wakes shed from the bars of the regular grid have a turbulence intensity that is greater than that of the cylinder wake. Hence, the FOV investigates a region where two wakes are competing against each other to entrain fluid from one and another, a process such as this is highly intermittent (cf. Baj & Buxton 2019) and results in much greater variation of mean flux. This suggests a larger number of shedding cycles need to be experimentally captured in order to attain convergence. Furthermore, the role of the turbulence intensity level in the wake could be to act as a critical point, beyond which a net mass detrainment is possible.

The behaviour of flux with respect to subjected length scale is much less clear and is seen as a secondary parameter with regards to its influence on entrainment flux. The lack of correlation is evident in figure 14(*b*). The group 3 cases are the most noticeable as they display a significant variation in the mean flux value for nearly the same integral length scale. This is mainly down to the extreme background turbulence that these runs

are subjected to. The large observed variation in flux for these group 3 cases is due to the lack of convergence, as explained in the previous paragraph.

3.4. *Turbulence parameter*

Several investigators in the past have used the turbulence parameter in an attempt to reconcile the effects of both length scale and turbulence intensity in a single form. A slightly modified version of the original parameter initially used by Taylor (1936), is

$$T_p = (TI)^m \left(\frac{L_{12}}{d}\right)^n. \tag{3.2}$$

Running an optimisation algorithm to calculate the best linear correlation between T_p and mean normalised flux produces the coefficients, $m = 1.28$ and $n = -0.11$. An increase of only 2 % in the coefficient of determination is achieved when comparing it to a linear fit based on the turbulence intensity alone. Therefore, it is clear to see that the dependence of entrainment behaviour in the far-wake region is mainly on the turbulence intensity of the incoming free-stream turbulence. The optimal coefficients clearly encourage the influence of TI, whilst providing only a weak inverse correlation to L_{12}. Hence, this clears the hazy dependencies suggested in previous literature.

3.5. *Multi-scale effects of free-stream turbulence*

The box counting method (Mandelbrot 1983) was utilised to investigate the scale by scale behaviour of the wake boundary under the influence of incoming free-stream turbulence. This method involves counting the number of boxes that are covered by a contour in a range of grids with increasing box sizes. Figure 17(a) presents results of the box counting method for the wake boundary. Note that Δ represents the length of one side of the square box. It was previously shown that an increase in the intensity of the background turbulence leads to an increased interfacial tortuosity. With respect to group 3, figure 17(a) shows an increase in length of the wake boundary as a result of the background turbulence occurs at all length scales and no single part of the spectrum is especially affected. It can also be seen from figure 17(a) that runs in groups 1 and 2 remain similar to the no-grid case with respect to the length of the wake boundary. The gradient of this plot can be used to evaluate the fractal dimension. Fractal dimensions lie between 1.14 and 1.23 for all runs and tend to increase with increased background turbulence intensity (figure not shown for brevity). Note that these values are similar to a fractal dimension of 6/5 that has been previously reported by Zhou & Vassilicos (2017) and Breda & Buxton (2019) for TNTIs.

In order to establish the effects of free-stream turbulence on entrainment on a scale by scale basis, a multi-scale analysis based on filtering of the high resolution dataset was conducted. A methodology inspired by that of Mistry *et al.* (2016) was implemented to do the same, which is illustrated in figure 18. The spatial filtering of the velocity data was conducted as per the procedure of Philip *et al.* (2014). The velocity fields were spatially filtered using box filters in the range $0.02d \leq \Delta \leq 0.60d$. With respect to the Taylor length scale (λ) calculated using the no-grid case, the box filter sizes were in the range $0.1\lambda_{no\ grid} \leq \Delta \leq 2.6\lambda_{no\ grid}$. Note that the Taylor scale has been calculated using the following expression, $\lambda_{no\ grid} = \sqrt{10\nu k/\varepsilon}$, where k is the turbulent kinetic energy and ε is the dissipation rate calculated using an assumption of local axisymmetry. To obtain the quoted value, the equation is averaged both spatially and temporally for all points that lie inside the wake. Furthermore, the wake boundary, as identified from the unfiltered

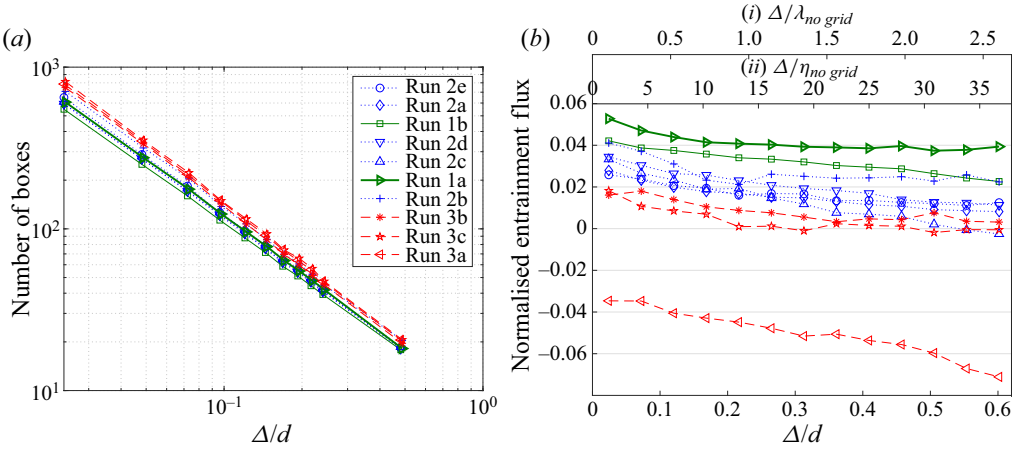

FIGURE 17. Multi-scale analysis. (*a*) Number of boxes covered by the wake boundary as a function of the box size used. (*b*) Scale by scale normalised entrainment flux. Note, the two axes on the top of the plot represent the filter size normalised by (*i*) the Taylor length scale (λ) and (*ii*) the Kolmogorov length scale (η) found inside the wake, when calculated for the no-grid case.

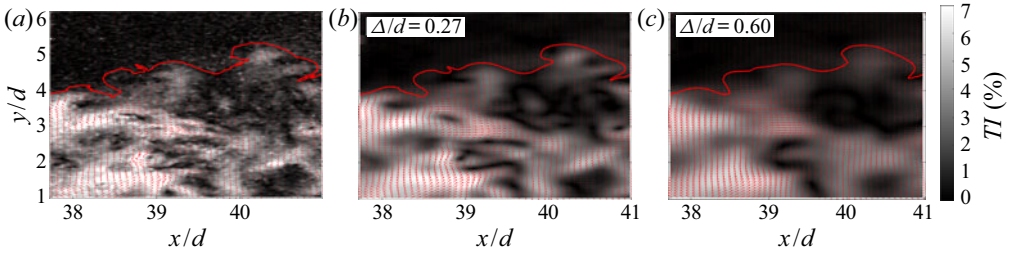

FIGURE 18. Illustration of the filtering process conducted for the multi-scale analysis. Plots depict the turbulence intensity field superimposed by velocity vectors and the wake boundary for the no-grid case. Note that only one in three velocity vectors are displayed for clarity. (*a*) Unfiltered. (*b*) Filter size $\Delta/d = 0.27$. (*c*) Filter size $\Delta/d = 0.60$.

PLIF light intensity data, was filtered using a moving average filter of span, Δ, to produce a filtered wake boundary. Examples of the filtered velocity fields superimposed by the filtered wake boundary can be found in figure 18 for three different filter sizes. Figure 18(*a*) depicts the unfiltered case, whereas figures 18(*b*) and 18(*c*) show the same for increasing filter sizes. Upon conducting the spatial filtering, the entrainment mass flux relative to the filtered wake boundary was calculated in the same manner as described in § 3.3 and the scale by scale flux result is depicted in figure 17(*b*). Firstly, examining the no-grid case, the mean entrainment mass flux remains at a constant level across the range of scales with a slight drop being witnessed at the smallest scales. This result correlates well with the analysis of Mistry *et al.* (2016) and demonstrates a largely constant rate of entrainment across all length scales. The remaining runs in groups 2 and 3 do show a gradual yet slight reduction in normalised entrainment flux as filter size is increased. However, in the global picture, this slight reduction is not significant when compared to the turbulence effect on entrainment and it is safe to say that the free-stream turbulence affects entrainment through

all scales and is not limited to the energy containing scales. This perhaps explains the weak dependence of the total entrainment flux on the integral length scale of the free-stream turbulence.

4. Conclusions

The effects of length scale and turbulence intensity in the background turbulence on the entrainment process as well as the bounding interface were evaluated using simultaneous PIV and PLIF experiments conducted in the far wake of a circular cylinder. The classical result from turbulent/non-turbulent interfaces of an enstrophy jump at the interface can still be seen when turbulent rotational fluid is available on both sides of the interface, therefore proving the existence of the turbulent/turbulent interface, something that was questioned in the review of da Silva *et al.* (2014). Additionally, background turbulence does act to increase the shear rate at the interface as long as the incoming turbulence is not too overpowering (does not reside in group 3). Furthermore, it was found that the entrainment process is largely sensitive to turbulence intensity of the incoming grid turbulence. An attempt to collectively analyse the effects of length scale and turbulence intensity through the use of the turbulence parameter resulted in power coefficients that greatly promoted the influence of TI, whilst being inversely correlated in a weak manner to L_{12}. We thus clear the hazy dependencies as suggested in the literature, showing that background turbulence intensity is the dominant parameter in influencing entrainment behaviour in the far wake.

Despite the presence of background turbulence leading to an increase of interface surface area, a net reduction in entrainment flux is observed with increased background turbulence intensity. By showing that an increased level of background turbulence concurrently leads to an increased interface surface area yet also a reduced entrainment rate, it was possible to discount the process of turbulent diffusion as being solely responsible for entrainment in the TTE paradigm. Rather, the reduction in entrainment was found to be an action of high intermittency. This was mainly through the stimulation of large, intermittent, but infrequent detrainment events that reside in the left tail of the mass flux PDF, as well as a suppression of similar net positive-entrainment events. In the most extreme case, where the background itself consisted of a strong wake, net detrainment was found to occur. The increase in entrainment that could be expected for the increased interfacial surface area is overbalanced towards the detrainment side by the highly infrequent yet highly powerful entrainment and detrainment events. The altered entrainment behaviour when free-stream turbulence intensity is greater than that of the wake itself is similar to the behaviour noticed by Ching *et al.* (1995) in the case when applied background turbulence intensity was comparable to the plume convective velocity. Finally, it was found that the influence of free-stream turbulence on entrainment behaviour is not just limited to the energy containing length scales, instead the effect is seen across all length scales thus justifying the weak dependence on L_{12} and showing that turbulent/turbulent entrainment is truly a multi-scale phenomenon.

Acknowledgements

The authors would like to acknowledge the financial support given by the Engineering and Physical Sciences Research Council through Grant No. EP/R512540/1. We are grateful to Dr H. Burridge for his helpful comments on an early draft of the manuscript. The authors would also like to note that preliminary results of this study were presented at the Eleventh International Symposium on Turbulence and Shear Flow Phenomena (TSFP11)

held in Southampton, UK, between the dates of 30 July and 2 August, 2019 (Kankanwadi & Buxton 2019).

Declaration of interests

The authors report no conflict of interest.

Supplementary movies

Supplementary movies are available at https://doi.org/10.1017/jfm.2020.755.

Appendix A. Flow downstream of turbulence generating grids

Figures 19–22 depict the turbulence intensity field as well as the locations of the field of view for all conducted runs. Note that, in all figures, the position of the cylinder as well as the extent of the field of view is clearly highlighted. In the cases where multiple run configurations are shown in the same figure, the cylinder and the boundary of the field of view are colour matched.

Appendix B. Further validation of wake boundary detection methodology

To further validate the experimental methodology utilised to identify the wake boundary, conditional enstrophy jumps calculated using two different approaches are compared. A light intensity gradient based methodology, as used in this experiment, is validated against a vorticity boundary calculated by examining enstrophy gradients. Note that the latter is a good control case as it is independent of the PLIF experiment. A comparison of this kind is only meaningful if the background flow lacks a significant amount of rotational flow. Therefore, this validation is conducted on the dataset produced from the no-grid case (run 1a).

Experimental vorticity data are inherently very noisy and hence finding a continuous contour of enstrophy across the entire field of view is not consistently possible. Therefore, a median filter is applied to the velocity vectors prior to the calculation of vorticity. Furthermore, a median filter is also applied to the resulting enstrophy to produce an enstrophy field that is conducive to evaluating a continuous contour along the wake boundary. However, not all snapshots are utilised in the evaluation of the figures below. In several cases the contour identifies an internal interface in the bulk of the wake. Hence, all snapshots where the mean difference between the contours using the two different methodologies are greater than a chosen threshold are discarded from the validation process. Note that the sensitivity to this threshold is also investigated and reported in figure 23.

Examining the behaviour of normalised enstrophy for all cases displayed in figure 23, it is evident that the sharp rise in the metric occurs at the same region of $\gamma = 0$ regardless of the size of the dataset chosen to be examined. However, discrepancies do exist between the two conditional plots and this is especially evident by examining the correlation near the enstrophy peak. This lack of correlation should be expected as our current experimental methodology can only collect a single component of vorticity. Visual examination of the snapshots reveals instances where the scalar extent is greater than that of the concentrated bulk of vorticity, hence resulting in a reduced peak of mean enstrophy just inside the scalar boundary. Despite the lack of correlation at the peak, the jump at $\gamma = 0$ in this analysis combined with the respective conditional jumps for enstrophy as well as PLIF

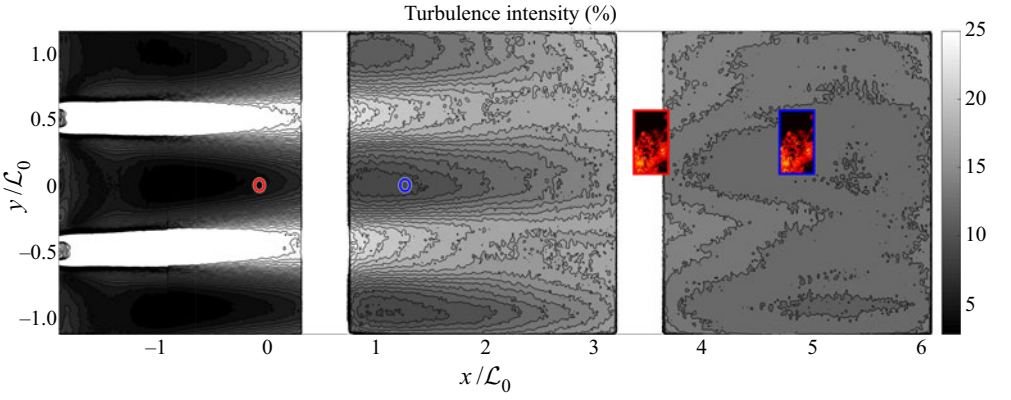

FIGURE 19. Turbulence intensity profile downstream of a square regular grid with $\mathcal{L}_0 = 111$ mm. The overlays represent the investigated FOVs. The positioning of the grid, cylinder and the experimental FOV are consistent with that of runs 3b and 3c for the red outline, whereas the blue outline highlights the positioning for run 3a.

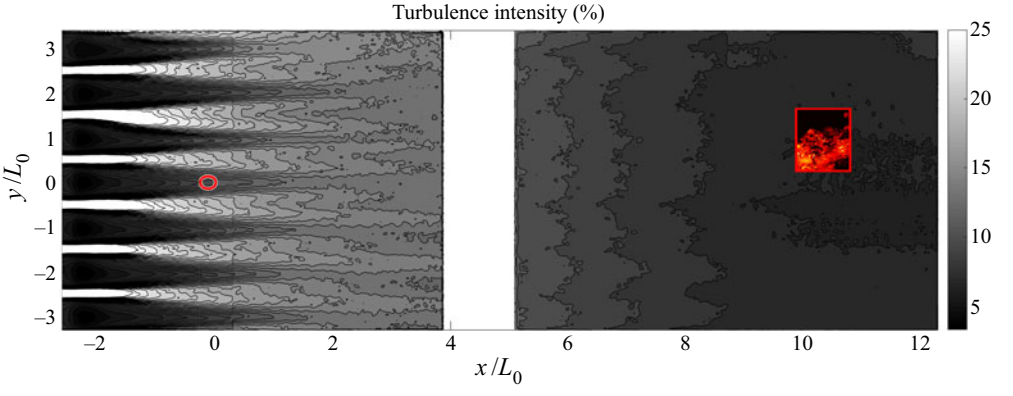

FIGURE 20. Turbulence intensity profile downstream of a square regular grid with $\mathcal{L}_0 = 38$ mm. The overlays represent the investigated FOVs. The positioning of the grid, cylinder and the experimental FOV are consistent with that of run 2b.

light intensity proves that the scalar is faithfully mixed within the entire extent of the wake.

Appendix C. Data clean up: removing unphysical entrainment velocity vectors from the entrainment mass flux calculation

The data cleaning process is designed to ensure that the final entrainment mass flux result is a true reflection of the physical phenomenon and is not adversely affected by numerical or algorithmic artefacts. Firstly, the baseline procedure disregards snapshots that do not include the wake boundary covering the full extent of the field of view. The data cleaning process is then implemented on this subset of snapshots. Prior to outlining this process, it is important to address its necessity. Unphysical entrainment velocity vectors creep into the algorithmic procedure when the contour that is identified as the wake boundary drastically changes shape between two consecutive snapshots.

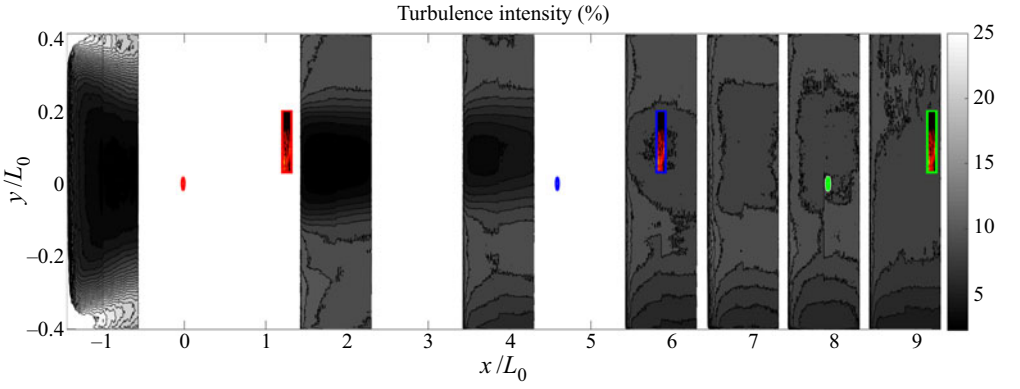

FIGURE 21. Turbulence intensity profile downstream of a square fractal grid with $\mathcal{L}_0 = 312$ mm. The overlays represent the investigated FOVs. The positioning of the grid, cylinder and the experimental FOV as defined by the red outline are consistent with that of run 1b. The blue outline represents run 2c, whereas the green outline represents run 2d.

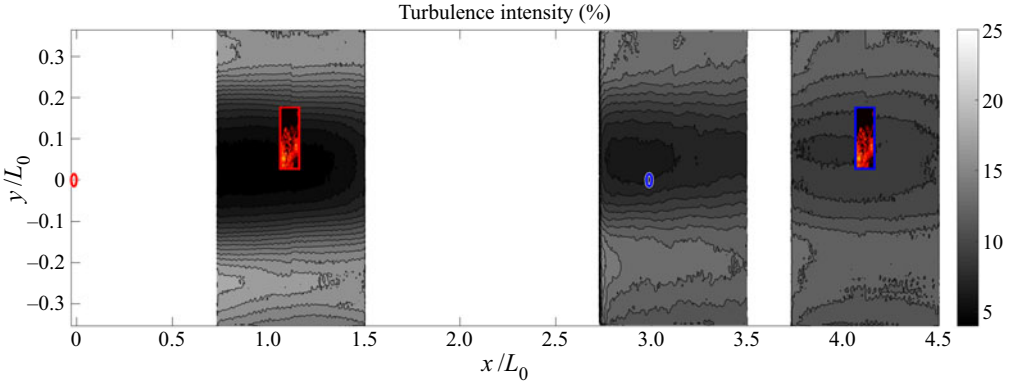

FIGURE 22. Turbulence intensity profile downstream of a square fractal grid with $\mathcal{L}_0 = 354$ mm. The overlays represent the investigated FOVs. The positioning of the grid, cylinder and the experimental FOV are consistent with that of run 2a for the red outline. Whereas the blue outline highlights the positioning for run 2e.

This may occur when an overhanging eddy either leaves or enters the field of view between a pair of snapshots. As the treatment mechanism identifies the point that is furthest away from the core of the wake to represent the wake boundary, this can lead to a misleading result that claims a large amount of either entrainment or detrainment. This process is illustrated in figure 24. Similarly, large additions and removals from the instantaneous wake interface may also occur when a 'three-dimensional reconnection event' or a traversal of a wake structure in the form of a 'teacup handle' is captured in the two-dimensional investigation plane. Therefore, these instances need to be rejected from the flux calculation. Furthermore, the entrainment velocity vectors that are calculated in the near vicinity of any artificial cliffs also need to be accounted for. In order to eliminate any invalid vectors that can arise due to the reasons specified above, the following steps were taken.

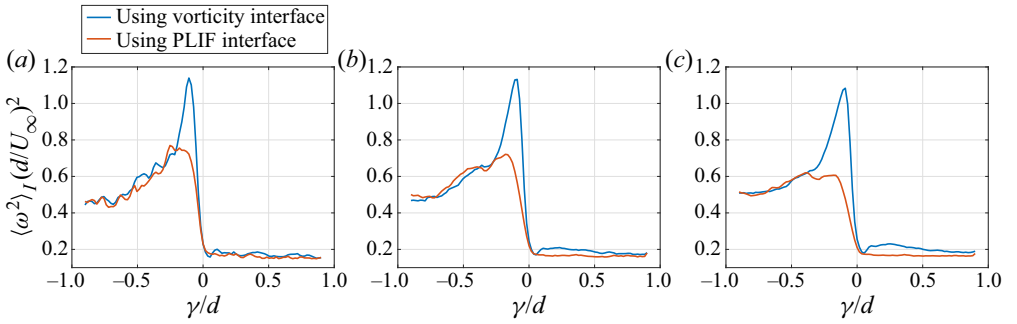

FIGURE 23. Interface conditioned statistics as a function of normal distance away from the wake boundary identified by both the PLIF data as well as the vorticity data. The series of figures illustrate the sensitivity to the chosen threshold. Captions of each panel represent the chosen threshold difference between the contours identified using the two different methodologies as well as the number of valid snapshots that consist of valid contours using both methodologies and pass the threshold test. (*a*) Threshold = 1 mm, valid snapshots = 73. (*b*) Threshold = 2.5 mm, valid snapshots = 402. (*c*) Threshold = 4 mm, valid snapshots = 726.

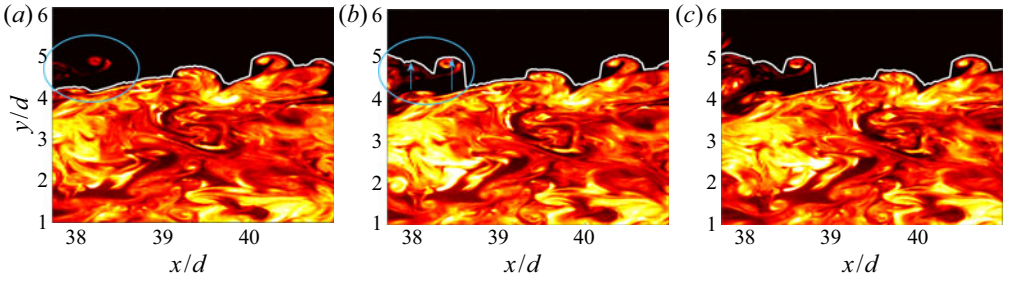

FIGURE 24. Artificial cliffs in the contour as a result of eddies entering the field of view. (*a*) Snapshot at time t_0. (*b*) Snapshot at time $t_0 + \Delta t$. (*c*) Snapshot at time $t_0 + 2\Delta t$.

(i) Using all snapshots that pass the baseline filter (as discussed above), a first pass of calculating the entrainment velocity vectors was conducted. This set of calculated velocity vectors was then used to evaluate a first pass mean (μ_{fp}) and standard deviation (σ_{fp}).

(ii) Next, a maximum and a minimal valid velocity magnitude was calculated using, Max&Min valid velocity = $\mu_{fp} \pm$ cutoff coefficient $\times \sigma_{fp}$. The selected cutoff coefficient for this study was equal to 2.4. Note that the value for this coefficient was carefully selected upon conducting a sensitivity study and ensuring that the mean entrainment mass flux was insensitive to a deviation of the cutoff coefficient in the neighbourhood of the selected value. These limits were used to produce a subset of valid entrainment velocity vectors.

(iii) The vectors that were located adjacent to artificial cliffs were considered to be invalid.

(iv) Finally, any snapshot that had greater than 40 % invalid vectors, was discarded from the flux calculations. Note that a similar sensitivity study as above was conducted for the 40 % value and a robust and insensitive percentage was chosen.

	Free-stream turbulence parameters		Experimental results		
Run	TI (%)	$\mathcal{L}_{12}/d$	Tortuosity	Mean normalised entrainment mass flux	Movie number
1a	1.4	0.3	3.54	0.052	1a
1b	2.9	1.2	3.19	0.042	1b
2a	5.8	2.4	3.47	0.028	2a
2b	7.0	0.7	4.06	0.041	2b
2c	7.9	2.0	3.58	0.032	2c
2d	8.1	2.6	3.45	0.034	2d
2e	9.1	2.3	3.80	0.026	2e
3a	12.8	1.0	4.64	−0.034	3a
3b	14.3	1.1	4.56	0.020	3b
3c	14.3	1.1			3c

TABLE 4. Tabulated experimental results alongside the relevant supplementary movie numbers.

Upon the completion of this process, the valid entrainment velocity vectors within each snapshot were integrated in segments that were split by any invalid vectors. The result of all of these segments were summed and the entrainment mass flux value for the snapshot was determined.

Appendix D. Supplementary movies of all conducted runs

Table 4 details a summary of results and also indicates the relevant supplementary movies available at https://doi.org/10.1017/jfm.2020.755 that contain a snippet of the data captured for all conducted runs. These movies depict the captured PLIF image with the identified wake boundary at the current time instance as well as the next time instance, superimposed on top of the image. A time series of entrainment mass flux as well as the mass flux PDF of the run are also shown in the view. Note that only 'valid' snapshots (see appendix C) are shown in the linked movies. The 'holes' in the time series represent snapshots where a valid wake boundary could not be identified.

REFERENCES

ARCOUMANIS, C., MCGUIRK, J. J. & PALMA, J. M. L. M. 1990 On the use of fluorescent dyes for concentration measurements in water flows. *Exp. Fluids* **10** (2), 177–180.

BAJ, P., BRUCE, P. J. K. & BUXTON, O. R. H. 2016 On a PLIF quantification methodology in a nonlinear dye response regime. *Exp. Fluids* **57** (6), 1–19.

BAJ, P. & BUXTON, O. R. H. 2019 Passive scalar dispersion in the near wake of a multi-scale array of rectangular cylinders. *J. Fluid Mech.* **864**, 181–220.

BETCHOV, R. 1956 An inequality concerning the production of vorticity in isotropic turbulence. *J. Fluid Mech.* **1** (5), 497–504.

BISSET, D. K., HUNT, J. C. R. & ROGERS, M. M. 2002 The turbulent/non-turbulent interface bounding a far wake. *J. Fluid Mech.* **451**, 383–410.

BREDA, M. & BUXTON, O. R. H. 2019 Behaviour of small-scale turbulence in the turbulent/non-turbulent interface region of developing turbulent jets. *J. Fluid Mech.* **879**, 187–216.

BUXTON, O. R. H., BREDA, M. & DHALL, K. 2019 Importance of small-scale anisotropy in the turbulent/nonturbulent interface region of turbulent free shear flows. *Phys. Rev. Fluids* **4** (3), 1–17.

CHING, C. Y., FERNANDO, H. J. S. & ROBLES, A. 1995 Breakdown of line plumes in turbulent environments. *J. Geophys. Res.* **100** (C3), 4707–4713.

CORRSIN, S. & KISTLER, A. L. 1955 Free-stream boundaries of turbulent flows. *NACA Tech. Rep.* 1244.

EAMES, I., JONSSON, C. & JOHNSON, P. B. 2011 The growth of a cylinder wake in turbulent flow. *J. Turbul.* **12**, N39.

ELSINGA, G. E. & DA SILVA, C. B. 2019 How the turbulent/non-turbulent interface is different from internal turbulence. *J. Fluid Mech.* **866**, 216–238.

GASKIN, S. J., MCKERNAN, M. & XUE, F. 2004 The effect of background turbulence on jet entrainment: an experimental study of a plane jet in a shallow coflow. *J. Hydraul. Res.* **42** (5), 533–542.

HOLZNER, M. & LÜTHI, B. 2011 Laminar superlayer at the turbulence boundary. *Phys. Rev. Lett.* **106** (13), 134503.

KANKANWADI, K. S. & BUXTON, O. R. H. 2019 Turbulent entrainment from a turbulent background. In *11th International Symposium on Turbulence and Shear Flow Phenomena, TSFP 2019*, pp. 1–6. TSFP.

KWOK, K. C. S. 1986 Turbulence effect on flow around circular-cylinder. *J. Engng Mech.-ASCE* **112** (11), 1181–1197.

LAIZET, S. & VASSILICOS, J. C. 2012 Fractal space-scale unfolding mechanism for energy-efficient turbulent mixing. *Phys. Rev.* E **86** (4), 1–5.

MANDELBROT, B. B. 1983 *The Fractal Geometry of Nature*, p. 173. W. H. Freeman.

MELINA, G., BRUCE, P. J. K., HEWITT, G. F. & VASSILICOS, J. C. 2017 Heat transfer in production and decay regions of grid-generated turbulence. *Intl J. Heat Mass Transfer* **109**, 537–554.

MISTRY, D., PHILIP, J., DAWSON, J. R. & MARUSIC, I. 2016 Entrainment at multi-scales across the turbulent/non-turbulent interface in an axisymmetric jet. *J. Fluid Mech.* **802**, 690–725.

PHILIP, J., MENEVEAU, C., DE SILVA, C. M. & MARUSIC, I. 2014 Multiscale analysis of fluxes at the turbulent/non-turbulent interface in high Reynolds number boundary layers. *Phys. Fluids* **26**, 015105.

SADEH, W. Z. & BRAUER, H. J. 1980 A visual investigation of turbulence in stagnation flow about a circular cylinder. *J. Fluid Mech.* **99** (1), 53–64.

DA SILVA, C. B., HUNT, J. C. R., EAMES, I. & WESTERWEEL, J. 2014 Interfacial layers between regions of different turbulence intensity. *Annu. Rev. Fluid Mech.* **46** (1), 567–590.

SREENIVASAN, K. R., RAMSHANKAR, R. & MENEVEAU, C. 1989 Mixing, entrainment and fractal dimensions of surfaces in turbulent flows. *Proc. R. Soc. Lond.* A **421**, 79–108.

TAYLOR, G. I. 1936 Statistical theory of turbulence V-effect of turbulence on boundary layer theoretical discussion of relationship between scale of turbulence and critical resistance of spheres. *Proc. R. Soc. Lond.* A **156** (888), 307–317.

TOWNSEND, A. A. 1976 *The Structure of Turbulent Shear Flow*. Cambridge University Press.

VAN REEUWIJK, M. & HOLZNER, M. 2013 The turbulence boundary of a temporal jet. *J. Fluid Mech.* **739**, 254–275.

VANDERWEL, C. & TAVOULARIS, S. 2014 On the accuracy of PLIF measurements in slender plumes. *Exp. Fluids* **55** (8), 1801.

WATANABE, T., SAKAI, Y., NAGATA, K., ITO, Y. & HAYASE, T. 2014 Vortex stretching and compression near the turbulent/non-turbulent interface in a planar jet. *J. Fluid Mech.* **758**, 754–785.

WESTERWEEL, J., FUKUSHIMA, C., PEDERSEN, J. & HUNT, J. C. R. 2005 Mechanics of the turbulent-nonturbulent interface of a jet. *Phys. Rev. Lett.* **95** (17), 1–4.

WILLIAMSON, C. H. K. 1996 Vortex dynamics in the cylinder wake. *Annu. Rev. Fluid Mech.* **28**, 477–539.

ZHOU, Y. & VASSILICOS, J. C. 2017 Related self-similar statistics of the turbulent/non-turbulent interface and the turbulence dissipation. *J. Fluid Mech.* **821**, 440–457.